Decoding homodimerization and antidepressant recognition at the norepinephrine transporter

Heng Zhang[1, *], Yuling Yin[2, *], Tianwei Zhang[2,3], Canrong Wu[1], Wen Hu[1,4], Xinheng He[1,5], Benxun Pan[2], Sanshan Jin[2], Qingning Yuan[1,4], H. Eric Xu[1,5†], and Yi Jiang[2,3,†]

1 The State Key Laboratory of Drug Research, Shanghai Institute of Materia Medica, Chinese Academy of Sciences, Shanghai 201203, China

2 Lingang Laboratory, Shanghai 200031, China

3 School of Life Science and Technology, ShanghaiTech University, Shanghai 201210, China

4 The Shanghai Advanced Electron Microscope Center, Shanghai Institute of Materia Medica, Chinese Academy of Sciences, Shanghai 201203, China

5 University of Chinese Academy of Sciences, Beijing 100049, China

* These authors contributed equally: Heng Zhang, Yuling Yin

† Correspondences: yjiang@lglab.ac.cn (Y.J.); eric.xu@simm.ac.cn (H.E.X.)

Abstract

The norepinephrine transporter (NET) plays a pivotal role in regulating neurotransmitter balance and is critical for normal physiology and neurobiology. Dysfunction of NET has been implicated in numerous neuropsychiatric diseases including depression, anxiety, attention deficit hyperactivity disorder, and Parkinson's disease. Here we report cryo-EM structures of NET in apo and substrate-bound forms, as well as complexes with six antidepressants. The structures reveal an unexpected NET dimer interface predominantly mediated by cholesterol and lipid molecules. The substrate norepinephrine is found to bind deep within the central binding pocket, with its amine group interacting with a conserved aspartate. The structures also provide insight into antidepressant recognition, including how subtle differences in binding poses confer selectivity over other monoamine transporters. Together these breakthrough findings significantly advance our understanding of NET regulation and inhibition, providing templates for designing improved antidepressants to treat neuropsychiatric disorders.

Introduction

Norepinephrine (NE) is an important neurotransmitter released from the presynaptic terminal to the synaptic cleft[1]. It stimulates specific receptors, such as the α- and β-adrenergic receptors[2], to regulate arousal, attention, cognitive function, and stress reactions[3-5]. The levels of monoamine neurotransmitters, including NE, dopamine (DA) and serotonin (5-HT), in the neural synapses, are controlled by their cognate monoamine transporters (MATs), including norepinephrine transporter (NET), dopamine transporter (DAT), and serotonin transporter (SERT). These MATs are secondary active transporters that belong to the solute carrier 6 (SLC6) transporter family and closely share their architecture and mechanistic properties[6-8]. Imbalance in neurotransmitter homeostasis is linked to a wide range of central nervous system disorders, including depression, attention deficit hyperactivity disorder, Parkinson's disease, anxiety and drug abuse[8, 9].

MATs are primary targets for psychostimulants and antidepressants. They inhibit the reuptake of monoamine neurotransmitters, thereby increasing their levels in the synaptic cleft[8, 9]. These antidepressants encompass selective serotonin reuptake inhibitors (SSRIs)[10], serotonin-norepinephrine reuptake inhibitors (SNRIs)[11], and norepinephrine reuptake inhibitors (NRIs)[12]. Recently, there has been extensive research on triple reuptake inhibitors (TRIs) due to their potential for improved efficacy, safety, and reduced tolerance in patients with major depressive disorder[13, 14]. However, there is still a lack of understanding regarding the binding profiles of antidepressants to all three MAT subtypes due to limited structural information, particularly the structures of human NET bound to diverse antidepressants. The absence of structural data for NET also hampers our comprehension of how it recognizes and transports natural substrates.

Both NET and SERT have been reported to associate with cholesterol-rich domains in brain tissue and transfected cell lines[15, 16]. Phosphatidylinositol-4,5-biphosphate (PIP2) facilitates NET dimerization and modulates substrate efflux [17]. Cholesterols and PIP2 have been identified as regulators of SERT function[18, 19]. Direct PIP2 binding mediates stable oligomer formation of SERT[20]. PIP2 also plays a crucial role in amphetamine-induced serotonin efflux[19], particularly in an oligomerization-dependent manner[21]. This suggests that cholesterols and lipids may play a role in regulating the oligomerization process. However, the precise mechanisms by which cholesterols and lipids regulate NET function and its oligomerization process remain poorly understood.

Structure models of human SERT[22-25] and *Drosophila* DAT (dDAT)[26-29] have offered valuable insights into transporters of serotonin and dopamine and the pharmacology of these transporter inhibitors. The structure of NET has been intensively pursued because

the structural data SERT and dDAT are insufficient to address the mechanism of NE recognition, NET oligomerization, and the roles of lipids in NET organization and activity. In this study, we report eight cryo-electron microscopy (cryo-EM) structures of human NET. These structures encompass its apo, the NE-bound, and six antidepressants-bound forms in the homodimeric state. Our research uncovers a homodimeric interface mediated by cholesterols and lipids. These structures also reveal atomic details of NE and antidepressant recognition, providing insights into substrate and antidepressant selectivity against MATs.

Results

Architecture of NET complexes

The wild-type full-length NET expressed in mammalian cells was utilized to assemble both apo and complexes bound to the natural substrate NE and six antidepressants. A total of eight distinct NET complexes were determined by the application of the cryo-EM method. These structures encompass apo and substrate NE-bound NET, as well as NET bound to six antidepressants (nisoxetine, atomoxetine, maprotiline, nomifensine, amitriptyline, and nefopam). These complexes were observed at a resolution of 2.9-3.4 Å in homodimeric forms (Fig. 1a-c, Extended Data Fig. 1, Supplementary Figs. 1-4). Seven out of eight structures of NET exhibit the outward-open conformation, and only the NE-bound NET structure is in an occluded state (Fig. 1d, Extended Data Fig. 1). The well-defined density of these structures enables precise modeling of ligands and the side chains of most residues except the N-terminus segment (M1-D52) (Extended Data Fig. 2). Several lipid molecules, including cholesterols, PIP2, and PI were built into final models based on the density map (Fig. 1a, Extended Data Fig. 2).

The dimeric assembly of the NET structure is distinct from monomeric forms of SERT and dDAT structures. However, the monomeric structure of NET is similar to SERT (PDB: 5I74) and dDAT (PDB: 4M48), adopting a canonical 12 transmembrane (TM) helices fold and cytosolic N- and C-termini, in which TMs 1-5 and TMs 6-10 form inherent pseudo-symmetry (Fig. 1c, Extended Data Fig. 3a). TM12 has a kink in the middle and is connected to the C-terminal latch, which is associated with intracellular loop 1 (IL1). TM1 and TM6 have broken into two segments, designated as TM1a-TM1b and TM6a-TM6b. The natural substrate NE and antidepressants occupy the central binding site halfway across the TMs, with two sodium (or one sodium in the NE-bound NET structure) and one chloride ion being located adjacent to inhibitors. The break regions of TMs 1 and 6 are also located near the central binding site and sculpt the binding pocket (Fig. 1c).

The most notable structural differences between NET, SERT, and dDAT are observed in their TMs 10-12, extracellular loop 2 (EL2), and the C-terminus (Extended Data Fig. 3b-d). In comparison to SERT, NET positions TM12 at a greater distance from TM10 and TM11, resulting in reduced stress on these helices and their corresponding outward movement (Extended Data Fig. 3b). This conformational change leads to EL6 being located further away from EL2 and brings about a subtle adjustment in the central binding site. Additionally, relative to SERT and dDAT, the longer EL2 of NET extends towards EL4, giving rise to a more compact extracellular lid (Extended Data Fig. 3c). At the intracellular side, the full-length NET allows the modeling of an extended C-terminus (E597-I617), a region that was typically truncated in the structures of SERT and dDAT. The 2-turn helix (E597-Q603) is positioned beneath and arranged in a reverse parallel configuration with the C-terminal latch (L584-T593). The remaining C-terminus contacts the C-terminal latch, the cytoplasmic ends of TM10 and TM11, and IL5, thus sealing the cytoplasmic ends of TMs 10-12 (Extended Data Fig. 3d). Considering the potential role of the C-terminal latch in protein kinase-mediated endocytic trafficking of DAT[30], this C-terminus segment may influence the regional conformation or accessibility to the cellular machinery for internalization.

NE bound at the central binding site

The NE binding site is located in the central binding cavity at halfway of TMs for the substrate and co-transported ions, sculpted by TMs 1, 3, 6, and 8 (Fig. 2a, b). Three subsites, denoted as A, B, and C, have been defined within the central binding site[31]. Subsite A, lined by TM1b, TM6 and TM8, is a polar region surrounding the conserved aspartate (D75 in NET), which facilitates the binding of monoamines by forming a salt bridge. Subsites B is sculpted by TM3 and TM8 to accommodate the aromatic ring moieties of monoamines and inhibitors. Subsite C, delimited by TM3, TM6a and TM10, include two aromatic residues (F317 and F323 in NET) to optimize the coordination of specific ligands by suitable isomerization.

The binding pose of NE is stabilized by several key interactions within three subsites of NET (Fig. 3a-c). Specifically, the primary amine of NE is anchored in subsite A, establishing a conserved hydrogen bond with the carboxylate of D75 (Fig. 2a). Replacing D75 with alanine abolished the neurotransmitter transporter activity of NET (Fig. 2c). The conserved aspartate is also critical for substrate uptake for DAT and SERT (Extended Data Fig. 4a)[27, 32]. The amine group also makes a polar interaction with the mainchain carbonyl of F317 (Fig. 2a). The β-OH group extends toward subsite A and points to F72, which made a substantial contribution to the NET activity (Fig. 2a, c).

The catechol group of NE predominantly binds to the subsite B cavity, sculpted by A145, V148, G149, Y152, S420, and G423 (Fig. 2b), with the *m*- and *p*-hydroxyl of the catechol group making polar interactions with S420 and the carbonyl of A145, respectively (Fig. 2a). The corresponding polar interactions are preserved between the *p*-hydroxyl group and A117 in the DA-dDAT structure and between the hydroxyl group in the indole ring of 5-HT and T439 in the 5-HT-SERT structure (Fig. 2d, e). The catechol ring of NE hydrophobically interacts with G423, A145, and V148 in subsite B and F323 in subsite C (Fig. 2a, b). Mutations in the subsites B and C cavities, especially in residues Y152 and F323, resulted in reductions in transporter activity (Fig. 2c).

Unlike substrates that bind to SERT and DAT in their outward-open states, NE binds to the occluded NET (Extended Data Fig. 4b-d). The overall binding pose of NE resembles that of DA in dDAT (PDB: 4XP1) and 5-HT in SERT (PDB: 7LIA) with the plane of its catechol group tilting ~17° and ~13° towards TM8 relative to the aromatic rings of the other two substrates (Fig. 2d, e, Extended Data Fig. 4b-d). In contrast, NE binds in a noticeably distinct pose relative to NE in NET-like dDAT. In the NET structure, the catechol ring of NE undergoes a 180-degree flip and inserts more deeply into subsite B when compared to the NET-like dDAT structure (Fig. 2f, Extended Data Fig. 4d).

The structural comparison of substrate-bound MATs offers valuable insights into the substrate selectivity of MATs. Although NE and DA are dual substrates for both DAT and NET, both NET and DAT preferably interact with DA with a higher affinity than NE. DA is translocated by NET about four-fold more efficiently than NE (*Km* values 0.67 μM for DA vs. 2.6 μM for NE). Similarly, DA is also a much better substrate for DAT than NE (*Km*=2.54 μM vs. 20 μM)[29]. From a structural aspect, the extra polar β-OH group of NE, which is the only structural difference of NE to DA, is packing against subsite A and constitutes a weak OH-π interaction with F72. However, in the DA-dDAT structure, the equivalent F43 in dDAT is positioned closer to the catechol ring of DA, resulting in a stronger edge-to-face π-π interaction (Fig. 2d). Thus, the differences in the β-OH group between DA and NE and their corresponding interactions with transporters could account for the greater transport efficiency of DAT and NET in transporting DA than NE.

In addition, relative to SERT, 5-HT is a weak substrate for NET. Compared to SERT, NET has a glycine at residue 149 whereas SERT has an alanine, which sidechain directly interacts with the indole ring of 5-HT and this interaction potentially increases the binding of 5-HT to SERT. The corresponding 5-HT/SERT interaction is not present in NET, which may explain the weak substrate of 5-HT for NET (Fig. 2e).

Substrate transport of NET

The structure of NE-bound NET enhances our understanding of the substrate transport mechanism of monoamine transporters[25, 31]. The transport is initiated when the transporter is in an outward-open conformation (Fig. 1d, Extended Data Fig. 5a, b). In this outward-open state, TMs 1b, 6a, 3, and 10 form a cone-shaped extracellular vestibule, providing a pathway for substrate and ions to access the central binding site (Extended Data Fig. 5a, b). Upon NE binding to the central site through the extracellular vestibule, TM1b and TM6a move toward the center of the transporter, effectively sealing off the extracellular vestibule, as demonstrated in the occluded conformation (Fig. 1d, Extended Data Fig. 5c). This conformational change subsequently triggers the unwinding of the intracellular segment of TM5, leading to the release of Na^+ at site 2 (Extended Data Fig. 5d-f). Additionally, it causes a prominent protrusion of the intracellular end of TM1a, facilitating the opening of the cytoplasmic cavity. These successive conformational changes enable the substrate to exit into the plasma, thus completing the substrate transport cycle, transitioning from the outward-open to occluded, and ultimately to the inward-open conformation[7, 31].

Binding of nisoxetine to the central binding pocket

Nisoxetine, a norepinephrine-selective reuptake inhibitor (NRI), shows ~230- to ~390-fold greater affinity for NET over SERT or DAT[33], despite the high sequence identity across MATs. Generally, nisoxetine is bulkier than the substrate NE and possesses a longer linker to the charged amino group, enabling it to snugly wedge into the central binding cavity to block NE from binding and effectively trap NET in the outward-open conformation.

The binding pose of nisoxetine is stabilized by extensive interactions with residues from the three subsites of NET (Extended Data Fig. 6a). In subsite A, the amine group of nisoxetine establishes a polar interaction with the carboxylate of the conserved D75. F72 is located beneath this amino moiety, forming a cation-π interaction, which is crucial for substrate transport (Fig. 3a). The polar interaction also involves Y152 from subsite B, which forms a hydrogen bond with D75 to coordinate a polar network with Na^+, Cl^-, and the amine of the inhibitor. Y152 is also engaged in a hydrophobic interaction with the methoxyphenoxy group, which fits into a hydrophobic subsite B formed by several residues including A145, V148, Y151, and A477. Consistently, Y151 and Y152 are important for substrate transport (Fig. 3a). Additionally, the hydroxyl moiety occupies subsite C and packs with F317 and F323 in TM6 (Fig. 3a). The potential clash between the aromatic moieties of nisoxetine and F341 and T497 in subsite C of SERT may lead to its low affinity to SERT (Extended Data Fig. 6b). Together, these interactions provide the basis for the high potency and selectivity of nisoxetine for NET.

Binding modes and MAT selectivity of antidepressants

We further analyze the binding modes of antidepressants and explore their potential selectivity for specific MAT subtypes. All antidepressants occupy the central binding site of NET with binding poses that partially overlap and exhibit similar interaction patterns with residues in the central binding site (Fig. 3b-f). Nevertheless, subtle variations in pocket components and antidepressant binding positions could still affect their selectivity for MAT subtypes.

Similar to nisoxetine, atomoxetine, and maprotiline are NET selective inhibitors[33, 34]. Their chemical structures and binding poses are highly similar to that of nisoxetine, with similar interactions with NET (Extended Data Fig. 6a, c). In contrast, amitriptyline, nomifensine, and nefopam are not NET selective inhibitors[33, 35]. Amitriptyline and nefopam are dual inhibitors of NET and SERT[33, 35], and their NET-bound structures reveal that these two inhibitors would be compatible with the SERT central pocket, but would bump into residues S149 and F326 in the DAT pocket (Extended Data Fig. 6d). Nomifensine is a dual inhibitor of NET and DAT but not for SERT[33], and the structure of nomifensine-bound NET complex reveal that nomifensine would fit well into the DAT pocket but not with the SERT pocket, with a potential collision with residues I172 and F335 in the SERT pocket (Extended Data Fig. 6e). Together, these structural observations thus offer valuable insights into understanding the selectivity of antidepressants for specific MAT subtypes.

Dimerization mediated by cholesterol and lipids

The unexpected observation of the NET homodimer provided an opportunity to examine the roles of oligomerization in the transporter activity of MATs. To gain insight into the mechanism of dimerization, we conducted a detailed investigation into the dimer interface using the nisoxetine-bound NET structure, which offers higher resolution compared to other available structures (Fig. 1a).

The NET homodimer is almost exclusively mediated by two layers of cholesterol packing (Fig. 4a, Extended Data Fig. 7). In the upper layer interface, there are six cholesterol molecules and two phosphatidylinositol (PI) molecules. The six cholesterol molecules are packed against TM4, TM9 and TM12, and form the core of the dimer interface in the upper layer. The two PI molecules are flanking the central cholesterol core interface (Fig. 4b). In the lower layer interface, there are also six cholesterol molecules, two PI molecules, and two PIP2 molecules. The bottom core interface is made up of the six cholesterol molecules, which are packed against each other and against TM3, TM4, TM9 and TM12. Flanking the cholesterol core interface are the two PI and the two PIP2, with their hydrophilic head groups forming polar interactions with NET (Fig. 4c, Extended Data Fig. 7c-h). In addition

to the lipid-mediated interface above, there are also direct intermolecular contacts by the spatially closed EL2 segment (H228-L232) and TM12, with L232 forming hydrophobic contacts with W553 in TM12 from the neighboring monomer (Fig. 4b). Together, these structural observations reveal a unique dimer interface predominantly comprised by cholesterols.

To assess the role of cholesterol in NET dimerization and transporter activity, we used methyl-β-cyclodextrin (MCD) to deplete cholesterols from the cell culture medium. The addition of MCD dramatically decreased the tendency for NET dimerization and transporter activity (Fig. 4d, e). Given that the depletion of cholesterols leads to a decrease in NET activity, it is reasonable to hypothesize that NET dimerization contributes to substrate transport activity.

Unique dimerization mode of NET

The unexpected homodimeric architecture of NET prompted us to examine whether DAT and SERT share a similar dimerization mode. However, sequence alignment showed low identity between NET and DAT/SERT in the dimer interface region (Extended Data Fig. 8a, b), indicating NET may have a unique dimerization mode compared to other MATs.

Previous studies suggest MATs can oligomerize through different interfaces [36]. For DAT, transmembrane helices 6, 11 and 12 constitute a putative dimer interface, with an intermolecular disulfide bond between C306 residues playing a key role [37]. A TM12-TM12 interface has also been proposed for SERT oligomers [38]. Notably, one report found DAT may form multiple dimer interfaces involving several TMs rather than a single defined interface, implying flexibility in DAT oligomeric assembly [36].

In contrast, our NET structure reveals a homodimer mediated primarily by cholesterols and lipids, a mechanism not previously observed (Fig. 4). Other transporters instead dimerize via transmembrane helix contacts or chaperone proteins. For example, the prokaryotic neurotransmitter symporter LeuT forms a homodimer using TM9, TM12 and EL2 (Extended Data Fig. 8c) [39]. The SLC12A4 dimer interface comprises both TMs and extracellular loops (Extended Data Fig. 8d) [40]. And SLC6A19 dimerization requires a chaperone (Extended Data Fig. 8e) [41].

Thus, our NET homodimer structure presents a unique cholesterol- and lipid-dependent interface distinct from other known transporter dimers. These variations highlight the versatility and complexity of interactions governing membrane protein oligomerization.

Further studies are needed to elucidate the functional and regulatory implications of the unanticipated NET dimer architecture.

Conclusion

The structures of human NET reveal insights into the transport mechanism, substrate recognition, inhibitor selectivity, and unexpected dimerization. The apo outward-open and norepinephrine-occluded structures delineate conserved structural rearrangements enabling the transport cycle. The ligand binding poses and comparisons rationalize selectivity differences between catecholamine neurotransmitters and closely related transporters. The inhibitor complexes illustrate how subtle binding mode variations confer selectivity among MATs.

Uniquely, NET forms a homodimer mediated by cholesterols and lipids, contrasting with other transporters dimerizing via protein-protein interactions. The cholesterol-dependent interface suggests a means of regulation not previously observed. Overall, by capturing multiple functional states and ligands, this comprehensive NET structure analysis fundamentally advances understanding of transport mechanisms, molecular recognition, and unanticipated dimerization architecture with implications for structure-based drug design.

Acknowledgments

The cryo-EM data were collected at the Advanced Center for Electron Microscopy, Shanghai Institute of Materia Medica (SIMM). We thank all staff at the institution for their assistance in cryo-EM data collection. This work was partially supported by the Lingang Laboratory, Grant No. LG-GG-202204-01 (Y.J. and H.E.X.); the National Natural Science Foundation (32171187 to Y.J., 82121005 to Y.J. and H.E.X., and 32130022 to H.E.X.), CAS Strategic Priority Research Program (XDB37030103 to H.E.X.); Shanghai Municipal Science and Technology Major Project (2019SHZDZX02 to H.E.X.); Shanghai Municipal Science and Technology Major Project (H.E.X.); the National Key R&D Program of China (2018YFA0507002 to H.E.X.).

Author contributions

H.Z. designed the expression constructs, purified the NET protein samples, prepared cryo-EM grids, calculated cryo-EM data, built and refined structural models, and prepared figures. Y.Y. conducted the functional studies and prepared figures. T.Z., B.P., and S.J. participated in functional studies and data analysis. C.W. participated in cryo-EM data calculation. W.H. and Q.Y. conducted cryo-EM data collection. X.H. analyzed structures. H.E.X. supervised the project, analyzed the structures, and modified the manuscript. Y.J.

initiated collaborations with H.E.X., supervised the project, and wrote the manuscript with inputs from all authors.

Competing interests

All authors declare no competing interests.

Data availability

All data is available in the main text or the supplementary materials. Materials are available from the corresponding authors upon reasonable request.

References

1 Caire MJ, Reddy V, Varacallo M. Physiology, Synapse. StatPearls. Treasure Island (FL) ineligible companies. Disclosure: Vamsi Reddy declares no relevant financial relationships with ineligible companies. Disclosure: Matthew Varacallo declares no relevant financial relationships with ineligible companies. 2023.

2 Ramos BP, Arnsten AF. Adrenergic pharmacology and cognition: focus on the prefrontal cortex. *Pharmacol Ther* 2007; **113**:523-536.

3 Pertovaara A. Noradrenergic pain modulation. *Prog Neurobiol* 2006; **80**:53-83.

4 Hurlemann R, Hawellek B, Matusch A *et al.* Noradrenergic modulation of emotion-induced forgetting and remembering. *J Neurosci* 2005; **25**:6343-6349.

5 Pignatelli M, Bonci A. Role of Dopamine Neurons in Reward and Aversion: A Synaptic Plasticity Perspective. *Neuron* 2015; **86**:1145-1157.

6 Kristensen AS, Andersen J, Jorgensen TN *et al.* SLC6 neurotransmitter transporters: structure, function, and regulation. *Pharmacol Rev* 2011; **63**:585-640.

7 Navratna V, Gouaux E. Insights into the mechanism and pharmacology of neurotransmitter sodium symporters. *Curr Opin Struct Biol* 2019; **54**:161-170.

8 Pramod AB, Foster J, Carvelli L, Henry LK. SLC6 transporters: structure, function, regulation, disease association and therapeutics. *Mol Aspects Med* 2013; **34**:197-219.

9 Rudnick G, Kramer R, Blakely RD, Murphy DL, Verrey F. The SLC6 transporters: perspectives on structure, functions, regulation, and models for transporter dysfunction. *Pflugers Arch* 2014; **466**:25-42.

10 Stahl SM, Lee-Zimmerman C, Cartwright S, Morrissette DA. Serotonergic drugs for depression and beyond. *Curr Drug Targets* 2013; **14**:578-585.

11 Lambert O, Bourin M. SNRIs: mechanism of action and clinical features. *Expert Rev Neurother* 2002; **2**:849-858.

12 Hajos M, Fleishaker JC, Filipiak-Reisner JK, Brown MT, Wong EH. The selective norepinephrine reuptake inhibitor antidepressant reboxetine: pharmacological and clinical profile. *CNS Drug Rev* 2004; **10**:23-44.

13 Shao L, Li W, Xie Q, Yin H. Triple reuptake inhibitors: a patent review (2006 - 2012). *Expert Opin Ther Pat* 2014; **24**:131-154.

14 Tu G, Fu T, Yang F *et al.* Understanding the Polypharmacological Profiles of Triple Reuptake Inhibitors by Molecular Simulation. *ACS Chem Neurosci* 2021; **12**:2013-2026.

15 Jayanthi LD, Samuvel DJ, Ramamoorthy S. Regulated internalization and phosphorylation

of the native norepinephrine transporter in response to phorbol esters. Evidence for localization in lipid rafts and lipid raft-mediated internalization. *J Biol Chem* 2004; **279**:19315-19326.

16 Magnani F, Tate CG, Wynne S, Williams C, Haase J. Partitioning of the serotonin transporter into lipid microdomains modulates transport of serotonin. *J Biol Chem* 2004; **279**:38770-38778.

17 Luethi D, Maier J, Rudin D *et al.* Phosphatidylinositol 4,5-bisphosphate (PIP(2)) facilitates norepinephrine transporter dimerization and modulates substrate efflux. *Commun Biol* 2022; **5**:1259.

18 Hamilton PJ, Belovich AN, Khelashvili G *et al.* PIP2 regulates psychostimulant behaviors through its interaction with a membrane protein. *Nat Chem Biol* 2014; **10**:582-589.

19 Buchmayer F, Schicker K, Steinkellner T *et al.* Amphetamine actions at the serotonin transporter rely on the availability of phosphatidylinositol-4,5-bisphosphate. *Proc Natl Acad Sci U S A* 2013; **110**:11642-11647.

20 Anderluh A, Hofmaier T, Klotzsch E *et al.* Direct PIP(2) binding mediates stable oligomer formation of the serotonin transporter. *Nat Commun* 2017; **8**:14089.

21 Seidel S, Singer EA, Just H *et al.* Amphetamines take two to tango: an oligomer-based counter-transport model of neurotransmitter transport explores the amphetamine action. *Mol Pharmacol* 2005; **67**:140-151.

22 Coleman JA, Green EM, Gouaux E. X-ray structures and mechanism of the human serotonin transporter. *Nature* 2016; **532**:334-339.

23 Coleman JA, Gouaux E. Structural basis for recognition of diverse antidepressants by the human serotonin transporter. *Nat Struct Mol Biol* 2018; **25**:170-175.

24 Coleman JA, Yang D, Zhao Z *et al.* Serotonin transporter-ibogaine complexes illuminate mechanisms of inhibition and transport. *Nature* 2019; **569**:141-145.

25 Yang D, Gouaux E. Illumination of serotonin transporter mechanism and role of the allosteric site. *Sci Adv* 2021; **7**:eabl3857.

26 Penmatsa A, Wang KH, Gouaux E. X-ray structure of dopamine transporter elucidates antidepressant mechanism. *Nature* 2013; **503**:85-90.

27 Wang KH, Penmatsa A, Gouaux E. Neurotransmitter and psychostimulant recognition by the dopamine transporter. *Nature* 2015; **521**:322-327.

28 Penmatsa A, Wang KH, Gouaux E. X-ray structures of Drosophila dopamine transporter in complex with nisoxetine and reboxetine. *Nat Struct Mol Biol* 2015; **22**:506-508.

29 Pidathala S, Mallela AK, Joseph D, Penmatsa A. Structural basis of norepinephrine recognition and transport inhibition in neurotransmitter transporters. *Nat Commun* 2021; **12**:2199.

30 Holton KL, Loder MK, Melikian HE. Nonclassical, distinct endocytic signals dictate constitutive and PKC-regulated neurotransmitter transporter internalization. *Nat Neurosci* 2005; **8**:881-888.

31 Cheng MH, Bahar I. Monoamine transporters: structure, intrinsic dynamics and allosteric regulation. *Nat Struct Mol Biol* 2019; **26**:545-556.

32 Wang H, Goehring A, Wang KH, Penmatsa A, Ressler R, Gouaux E. Structural basis for action by diverse antidepressants on biogenic amine transporters. *Nature* 2013; **503**:141-145.

33 Richelson E, Pfenning M. Blockade by antidepressants and related compounds of biogenic amine uptake into rat brain synaptosomes: most antidepressants selectively block norepinephrine uptake. *Eur J Pharmacol* 1984; **104**:277-286.
34 Bymaster FP, Katner JS, Nelson DL *et al.* Atomoxetine increases extracellular levels of norepinephrine and dopamine in prefrontal cortex of rat: a potential mechanism for efficacy in attention deficit/hyperactivity disorder. *Neuropsychopharmacology* 2002; **27**:699-711.
35 Gregori-Puigjane E, Setola V, Hert J *et al.* Identifying mechanism-of-action targets for drugs and probes. *Proc Natl Acad Sci U S A* 2012; **109**:11178-11183.
36 Jayaraman K, Morley AN, Szollosi D, Wassenaar TA, Sitte HH, Stockner T. Dopamine transporter oligomerization involves the scaffold domain, but spares the bundle domain. *PLoS Comput Biol* 2018; **14**:e1006229.
37 Cheng MH, Garcia-Olivares J, Wasserman S, DiPietro J, Bahar I. Allosteric modulation of human dopamine transporter activity under conditions promoting its dimerization. *J Biol Chem* 2017; **292**:12471-12482.
38 Periole X, Zeppelin T, Schiott B. Dimer Interface of the Human Serotonin Transporter and Effect of the Membrane Composition. *Sci Rep* 2018; **8**:5080.
39 Singh SK, Piscitelli CL, Yamashita A, Gouaux E. A competitive inhibitor traps LeuT in an open-to-out conformation. *Science* 2008; **322**:1655-1661.
40 Liu S, Chang S, Han B *et al.* Cryo-EM structures of the human cation-chloride cotransporter KCC1. *Science* 2019; **366**:505-508.
41 Yan R, Zhang Y, Li Y, Xia L, Guo Y, Zhou Q. Structural basis for the recognition of SARS-CoV-2 by full-length human ACE2. *Science* 2020; **367**:1444-1448.

Methods

Expression and purification of NET

The coding sequences for human wild-type NET(SLC6A2) were cloned into pEG BacMam vector that was a gift from Eric Gouaux lab. 1xFlag tags were located at the N termini of proteins and connected by a GGS linker. NET was expressed in HEK293S GnTI− cells cultured in Freestyle 293 Expression Medium (Gibco) supplemented with 2% fetal bovine serum (Gibco). Cells were collected by centrifugation (1,000 × g, 10 min, 4 °C) and disrupted by a Dounce tissue grinder (Merck Millipore) in buffer (50 mM HEPES pH7.5, 150 mM NaCl) supplemented with 10 μg/mL aprotinin, 4 μg/mL leupeptin, and 3 μg/mL pepstatin A (all from Yeasen Biotechnology (Shanghai) Co., Ltd). Cell debris was removed by centrifugation (8,000 × g, 25 min, 4 °C). The membrane fraction was collected by ultracentrifugation (100,000 × g, 1 h, 4 °C), and solubilized for 2.5 h at 4 °C in buffer (50mM HEPES pH7.5, 150 mM NaCl, 1% (w/v) n-dodecyl -D-maltoside (DDM, Anatrace), 0.1% (w/v) cholesteryl hemisuccinate (CHS, Anatrace)). Insoluble components were removed by centrifugation (30,000 × g, 1 h, 4 °C). The detergent-soluble fraction was incubated for 2 h at 4 °C with anti-DYKDDDDK G1 Affinity Resin (GenScript). The protein was then eluted by 0.2 mg/mL DYKDDDDK peptide (Genscript), and purified by size-exclusion

chromatography (SEC) on a Superdex 200 Increase 10/300 GL column (GE Healthcare), equilibrated with SEC buffer (20 mM HEPES pH7.5, 150 mM NaCl, 0.02% DDM, 0.002 %CHS). The peak fractions of the protein were collected and concentrated to 2.0 mg/mL, using a 100 kDa MWCO Amicon centrifugal filter (Merck Millipore).

Nanodisc-NET reconstitution

POPC:POPE:POPG lipid mix (3:1:1, Avanti Polar Lipids) was solubilized in chloroform, dried under argon gas to form a lipid film, and stored under vacuum overnight. The lipid film was resuspended at a concentration of 500 mM in buffer containing 20 mM Tris, pH 7.5, 100 mM NaCl, and 100 mM sodium cholate. NET, the MSP1D1 membrane scaffold protein, and lipids were mixed at a molar ratio of 1:2:10 in buffer containing 20 mM HEPES, pH 7.5, 100 mM NaCl, and 10 mM sodium cholate and incubated for 2 h at 4 °C. The Nanodisc formation was initiated by adding 180 mg/mL equilibrated Bio-Beads SM-2 resin (Bio-Rad) and under constant agitation overnight at 4 °C. The sample was submitted to SEC on a Superdex 200 Increase 10/300 column (GE Healthcare) equilibrated with SEC buffer (20 mM HEPES pH7.5, 150 mM NaCl). SEC peak fractions were pooled and concentrated to 1.5 mg/mL for cryo-EM sample preparation.

Grid preparation and data acquisition

For structure determination of NET-MSP1D1-apo or incubated with a final concentration of 100 μM ligands for 2 hours by single particle cryo-EM, 2.3 μL portion of the purified protein NET at a concentration of 1.2 mg/mL was applied to glow-discharged holy carbon grids (Quantifoil R1.2/1.3 Au 300 mesh). Excess liquid was removed in Vitrobot Mark IV (Thermo Fisher Scientific) under 8°C and 100% humidity conditions, by blotting grids for 4.5 seconds with a blotting force of 1. Grids were subsequently flash-frozen in liquid ethane.

The grid of NET-MSP1D1-Apo was transferred to a 300 kV Titan Krios G4 (FEI) equipped with a cold field emission gun (E-CFEG) and a Falcon 4i direct electron detector. Raw micrographs were collected with super-resolution 0.365 Å using EPU (2.13) at the Shanghai Advanced Center for Electron Microscopy. All datasets were recorded at a pixel size of 0.73 Å with a total dose of 50 e/ Å 2 for 36 frames. Raw images were aligned using the motion correction program MotionCor2.

Data processing

For the dataset of NET-MSP1D1-Apo, a total of 8,793 dose-weighted micrographs were imported into cryoSPARCv4.3.1, and contrast transfer function parameters were calculated by Patch CTF. Micrographs with a CTF resolution worse than 4 angstroms were discarded. A blob picker with a diameter of 150 Å was used for initial particle selection. After 8 rounds

of 2D classification, 41,355 high-quality particles were retained for 3D reconstitution and refinement. The class of about 4.5 Å density were selected as good references and imparted as good seeds for the Template picker. After several rounds of Seed-facilitated multi-reference 3D classification and resolution gradient classification, 171,068 particles were kept for nonuniform refinement and local refinement. The last, the map containing two units of NET with symmetry C2 resolved 3.29 Å (Supplementary Fig, 1).

Following a similar processing flow, for the dataset of NET-MSP1D1-Nisoxetine, a map containing two units of NET with symmetry C2 resolved 2.89 Å (Supplementary Fig, 1). For the datasets of NET-MSP1D1-Norepinephrine/Atomoxetine/Maprotiline/Nomifensin, the maps containing two units of NET with symmetry C2 resolved 3.24 Å, 3.29 Å, 3.29 Å and 3.13 Å. For the datasets of NET-MSP1D1-Amitriptyline/Nefopam, the maps containing two units of NET without symmetry resolved 3.00 Å and 3.15 Å (supplementary Figs. 2-4).

Model building and refinement

The initial NET structure model was generated by AlphaFold2. The model was then fitted into the density map in UCSF ChimeraX. With iterative manual adjustment and rebuilding in COOT, the model matched the density map more closely. Ligands restraint files were generated by PHENIX1.17_elbow. The generated models were refined against the corresponding maps in phenix.real_space_refine.

Neurotransmitter Transporter Uptake Assay

AD293 cells were transiently transfected with wild-type or mutant NET after being seeded into 6-well plates at a density of 400,000 cells/well in a volume of 2 mL and incubated at 37 °C in 5% CO2 for 24 h. The cells were then processed with 0.25% trypsin and re-seeded into the 384-well plate with 20,000 cells per well overnight. Followed by the neurotransmitter transporter uptake assay performed according to the instructions provided by the manufacturer of Molecular Devices (Explorer Kit R8173). Briefly, aspirate the medium from the wells, and pipet 25 μL/well of different concentrations of compound diluted in 1X HBSS and incubated at 37 °C for 30 min. Then each well was added with 25 μL of dye solution from the kit and incubated at 37 °C for 1 h. The signals were read on the Spark (Tecan) with an excitation wavelength of 440 nm and an emission wavelength of 520 nm. Data were normalized to the response of wild-type NET.

NanoBiT Assay

The analysis of NET homodimer was performed according to the NanoBiT system (Promega). LgBiT (17.6 kDa) and SmBiT (VTGYRLFEEIL) of the NanoBiT were fused to the N terminus of the expression clone of NET respectively. AD293 cells were transiently

co-transfected with the LgBiT and SmBiT NET at a 1:1 ratio. Cells transfected with LgBiT or SmBiT NET as well as NanoBiT-unfused NET at a 1:1 ratio were regarded as negative control. The cell density of transfection and the following re-seeded operation were the same as above described in the neurotransmitter transporter uptake assay. After the re-seeded cells in a 384-well plate overnight, aspirate the medium from the wells. Then pipet 20 μL/well different concentrations of methyl-β-cyclodextrin (MCD, Sigma) diluted in a medium containing 25 mM HEPES (Gibco) and incubated at 37 °C in 5% CO_2 for 1 h. Subsequently, each well was added with 10 μL of 10 μM coelenterazine (Yeasen) diluted in PBS. Luminescence was measured on EnVison (PerkinElmer).

For determination of transporter activity within NET homodimer, the group of LgBiT and SmBiT NET co-transfected cells were re-seeded into the 384-well plate. Then cells were processed with 25 μL/well MCD similar to the description above except that the substrate was replaced by 25 μL/well dye solution from Molecular Devices (Explorer Kit R8173) and signals were read on the Spark (Tecan) with excitation wavelength at 440 nm and emission wavelength at 520 nm. Data were normalized to the response of LgBiT and SmBiT NET co-transfected cells with 0 mM MCD treatment.

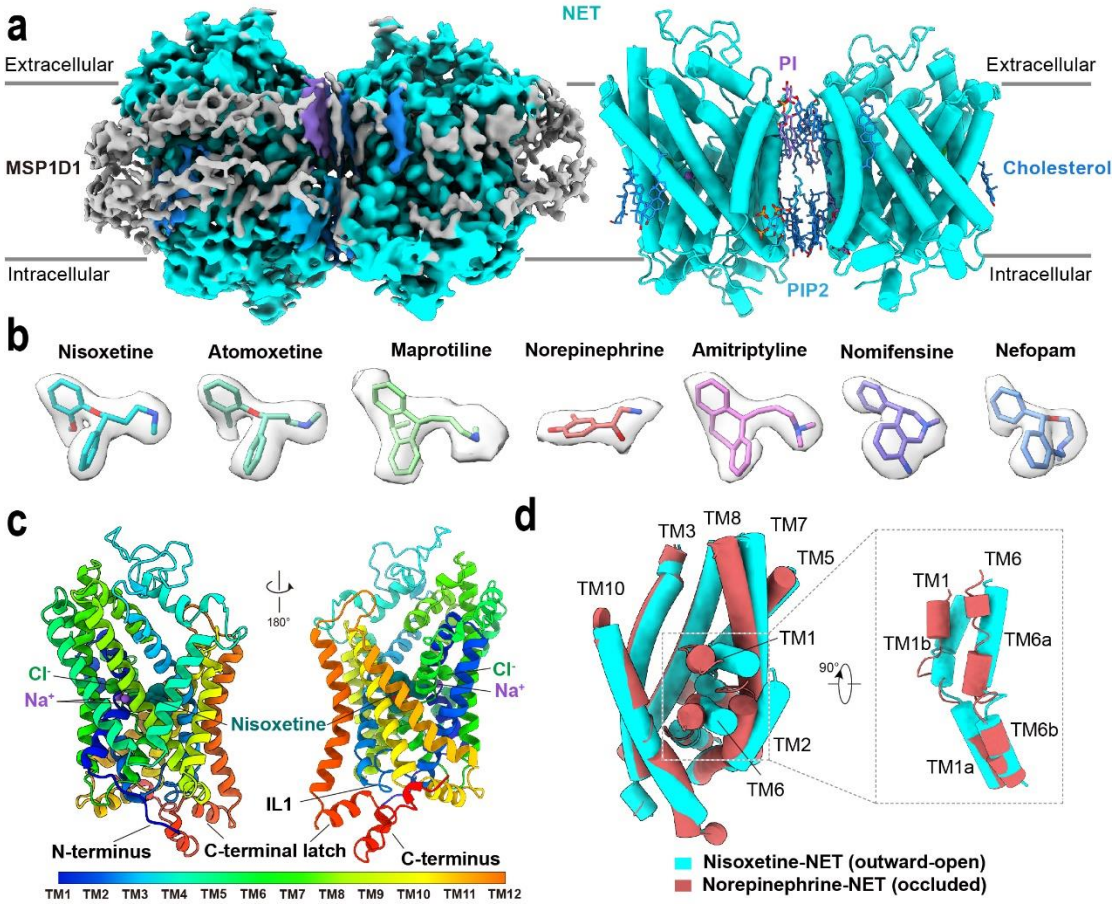

559

560

561 **Fig. 1 | Cryo-EM structures of NET complexes. a,** Cryo-EM density (left) and cylinder
562 presentation of the Nisoxetine-NET complex. The complex density map with the nanodisc
563 is shown at a level of 0.18 electrons per Å^3. **b,** Densities of natural substrate norepinephrine
564 (NE) and six antidepressants in the structures of NET complexes. **c,** the overall structure
565 of the nisoxetine-NET complex in the monomer form in cartoon representation. TMs are
566 colored as indicated. **d,** Conformational comparison of the nisoxetine-NET complex in the
567 outward-open conformation with the NE-NET complex in the occluded conformation.

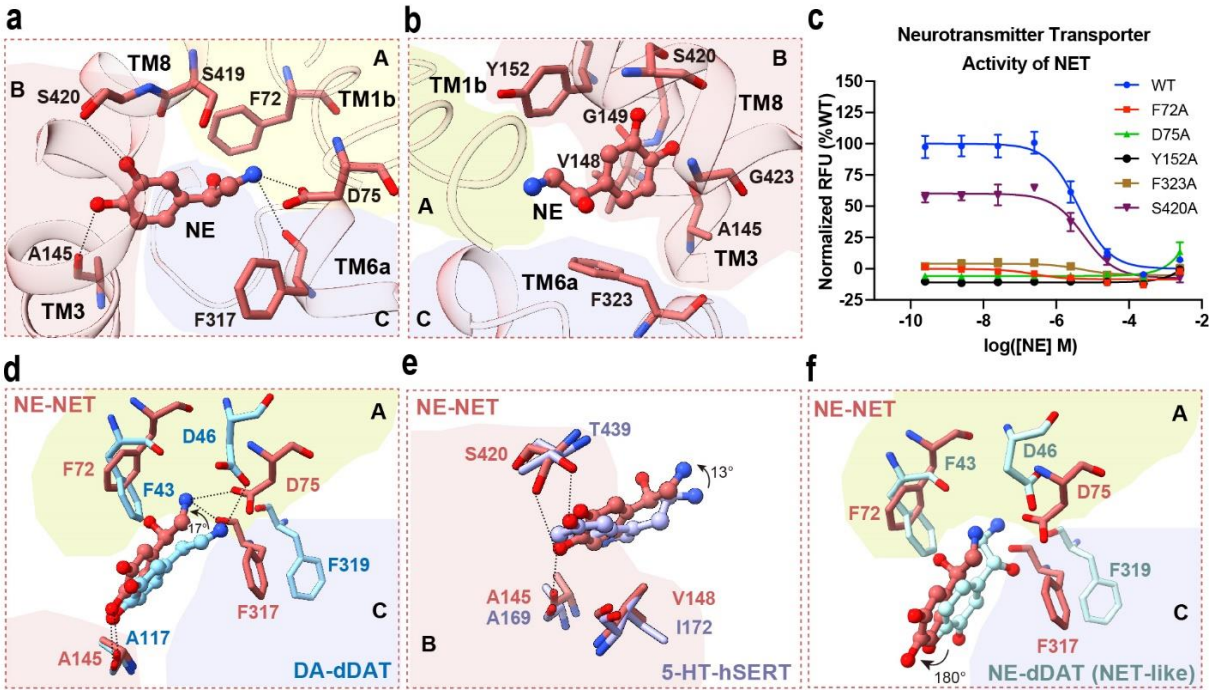

Fig. 2 | Recognition of NE by NET. a, b, Interactions of NE with residues in the central binding site of NET. The polar interactions are shown as black dashed lines. **c,** Effects of alanine mutagenesis on residues in the central binding site on NET transport activity. **d-f,** Comparisons in the binding pose of NE in NET with DA in dDAT (**d**, PDB: 4XP1), 5-HT in SERT (**e**, PDB: 7LIA), and NE in NET-like dDAT (**f**, PDB: 6M0Z). Subsites A, B, and C are highlighted with yellow, salmon, and light blue backgrounds, respectively. The substrates NE, DA, and 5-HT are represented in the ball-and-stick format. The side chains of amino acid residues in the monoamine transporters are depicted as sticks.

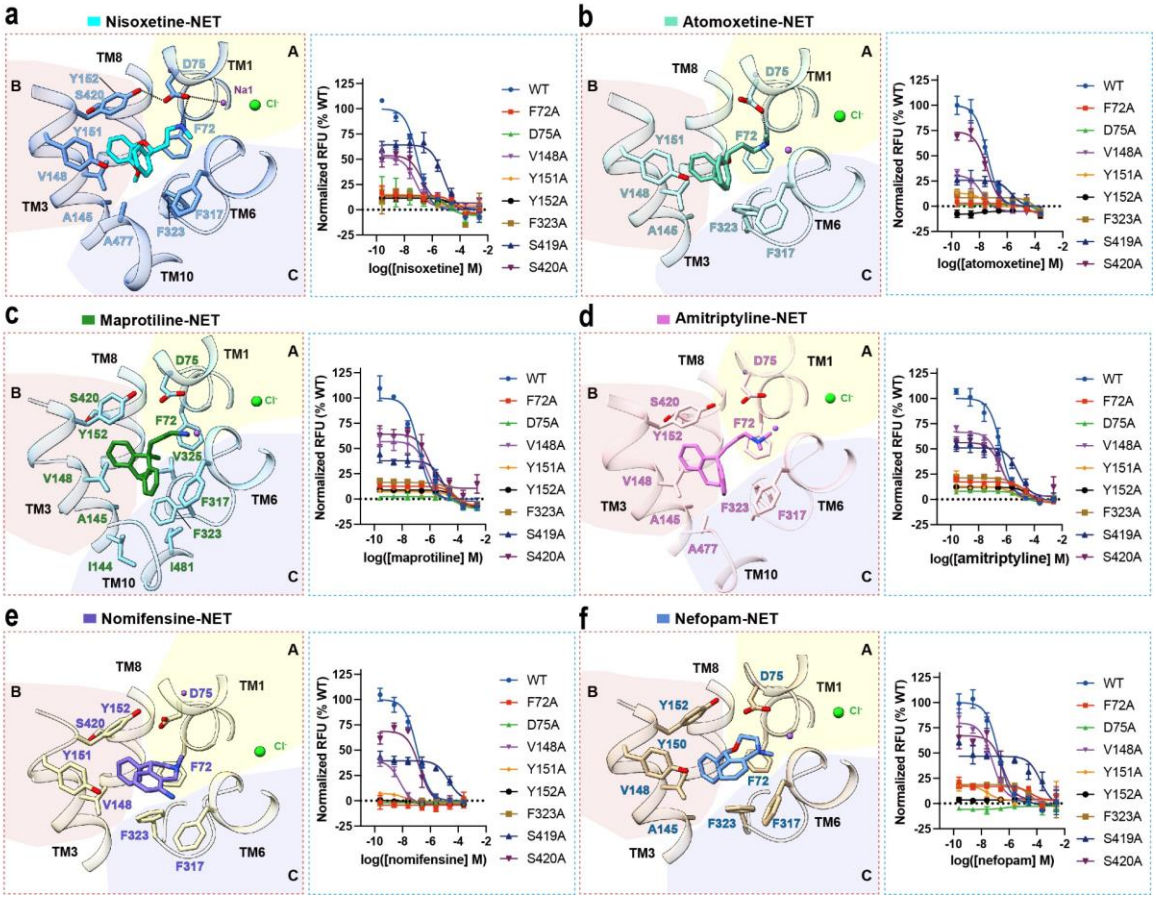

Fig. 3 | Recognition of antidepressants by NET. The interactions of antidepressants nisoxetine (**a**), atomoxetine (**b**), maprotiline (**c**), amitriptyline (**d**), nomifensine (**e**), nefopam (**f**) with residues in the central binding site of NET. Effects of alanine mutations in central binding site residues on the inhibition of NET transport activity by antidepressants. Each data point presents mean ± SD. WT, wild-type. Subsites A, B, and C are highlighted with yellow, salmon, and light blue backgrounds, respectively.

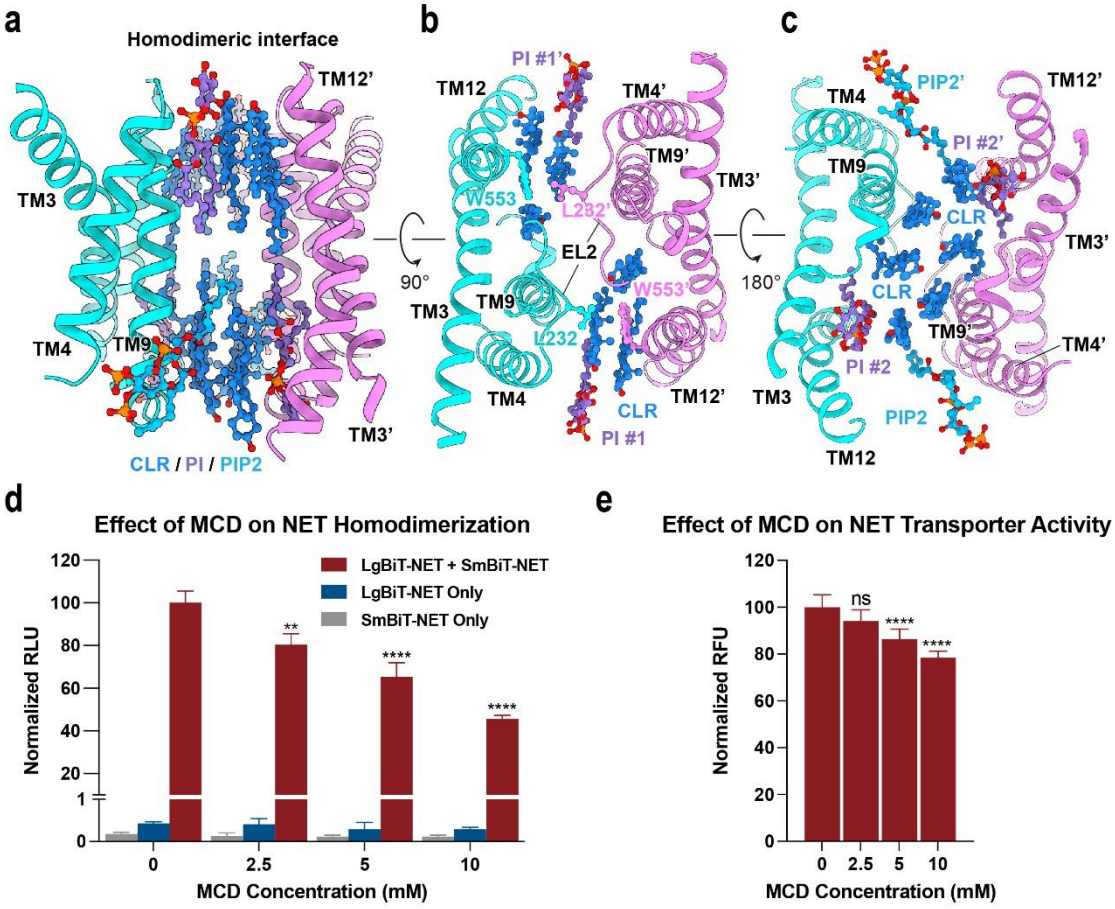

Fig. 4 | The NET homodimeric interface mediated by cholesterols and lipids. a-c, The NET homodimer is almost exclusively mediated by two layers of cholesterol packing, presented in the side view (**a**), the extracellular view (**b**), and the intracellular view (**c**). **d, e,** Effects of cholesterol depletion by MCD for NET homodimerization (**d**) and transporter activity (**e**). Each data point presents mean ± SD. Data were analyzed by one-way ANOVA with Dunnett's multiple comparisons test to show the significance compared with 0 mM MCD treated group, $^{**}P < 0.01$, $^{****}P < 0.0001$. ns, no significant difference.

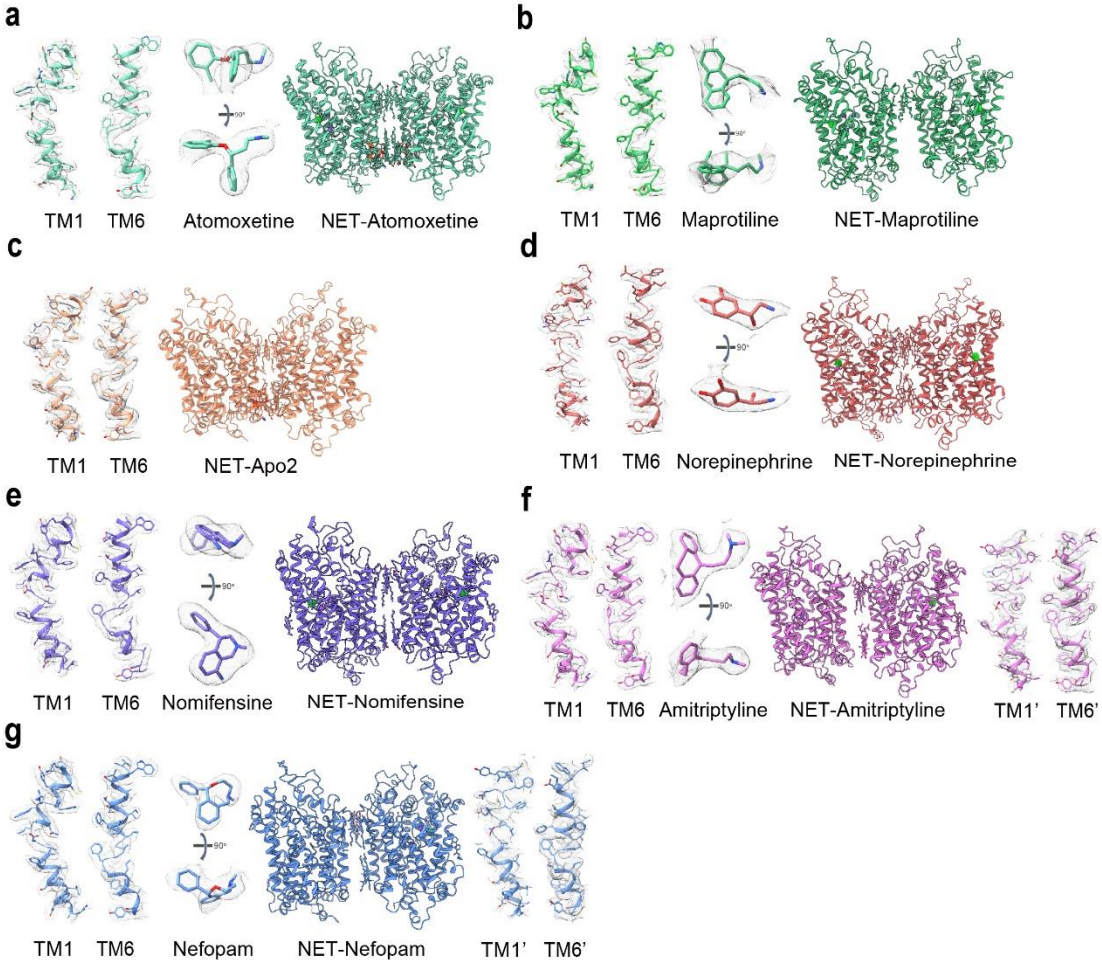

Extended Data Fig. 1| Cryo-EM structural determination of human NET in the apo state and bound to native substrate norepinephrine or inhibitors. a-e, The overall structures of Atomoxetine/Maprotiline/Apo/Norepinephrine bound NET dimers. The representative density maps of TM1, TM6, apo NET, and Atomoxetine/Maprotiline/ Norepinephrine-bound NET dimers are shown. **f-g,** The two protomers of NET-Amitriptyline/Nefopam dimer are asymmetric. The protomer containing amitriptyline or nefopam shows an outward-open state and exhibits better density, while the other protomer adopts an occluded conformation and lacks the density of inhibitors.

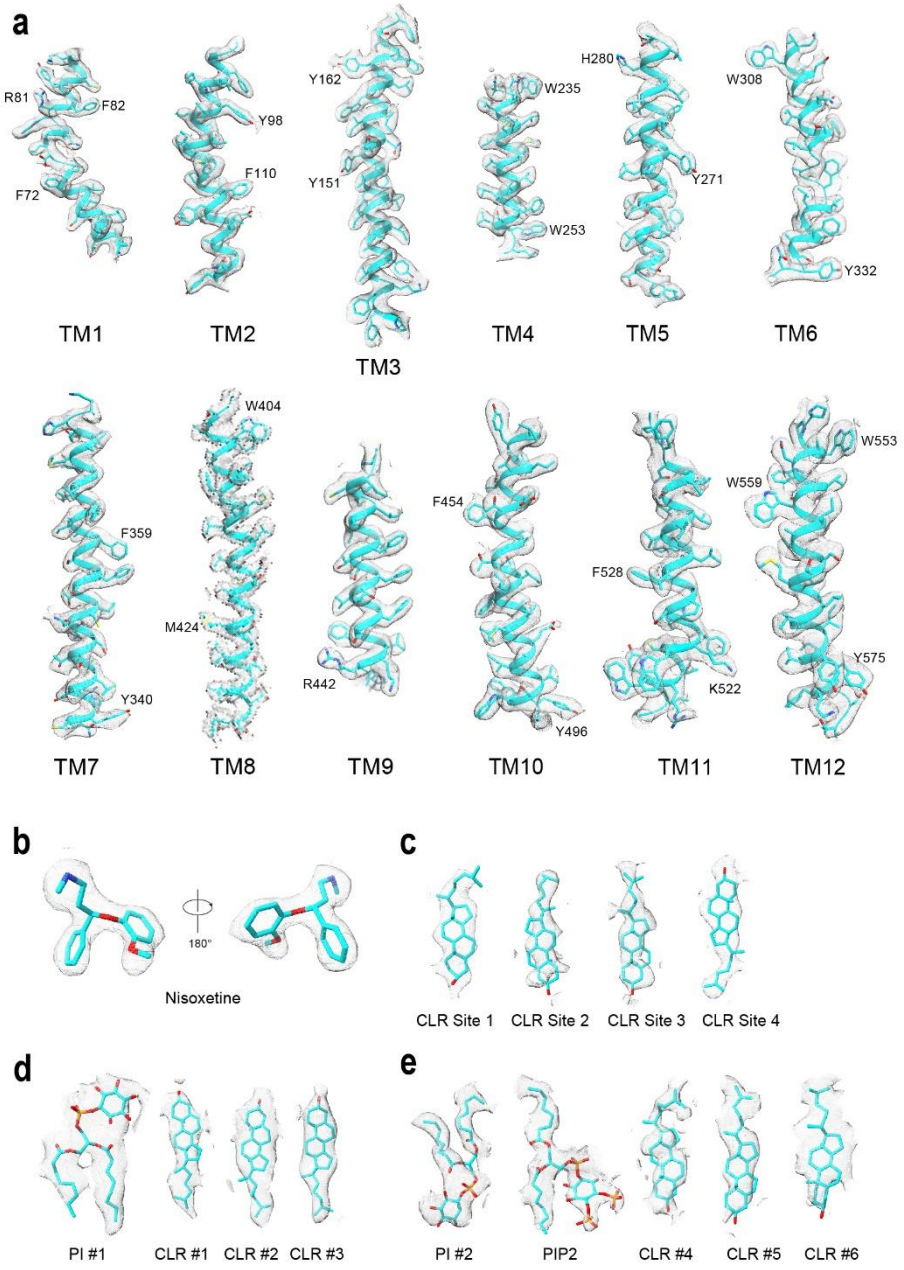

Extended Data Fig. 2| Representative EM densities of NET. a, Nisoxetine-NET dimer transmembrane helices and EM densities at a contour level of 0.30. **b,** Nisoxetine and EM densities at a contour level of 0.32. **c,** Cholesterols surround NET except for the dimer interface, EM densities at a contour level of 0.18. **d,** Lipid and cholesterols at the upper layer dimer interface, EM densities at a contour level of 0.20. **e,** Lipid and cholesterols at the lower layer dimer interface, EM densities at a contour level of 0.20.

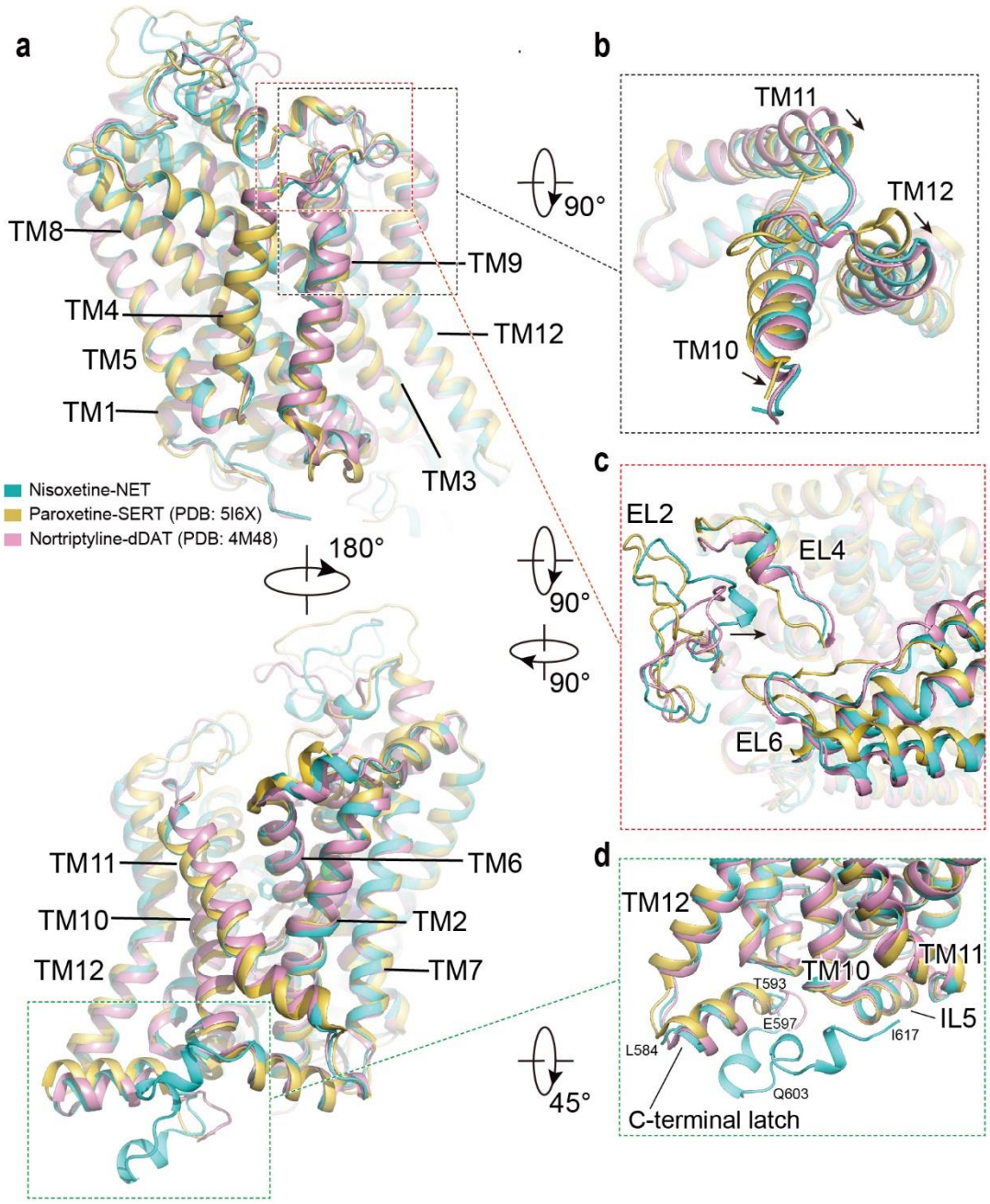

Extended Data Fig. 3| Structural comparisons of NET with SERT and dDAT in outward-open states. a, Structural comparisons of the nisoxetine-NET, paroxetine-SERT (PDB: 5I6X), and nortriptyline-dDAT (PDB: 4M48). **b,** Structural comparisons of the extracellular segments of TMs 10-12 in NET, SERT, and dDAT. The directional movements of TMs 10-12 in NET relative to that in SERT are indicated by black arrows. **c,** Comparisons of EL2, EL4, and EL6 among NET, SERT, and dDAT. The longer EL2 of NET relative to SERT and dDAT protrudes towards EL4, as indicated by the black arrow. **d,** The NET structure shows an extended C-terminus relative to SERT and dDAT. This extended C-terminus contacts the C-terminal latch, the cytoplasmic ends of TM10 and TM11, and IL5, thus sealing the cytoplasmic ends of TMs 10-12.

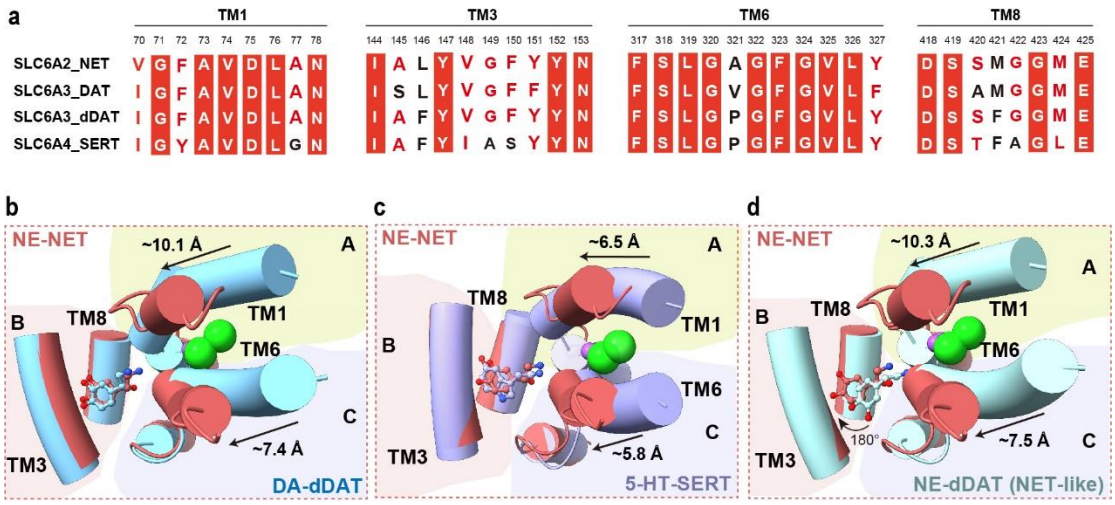

Extended Data Fig. 4| The comparison of substrate binding pockets of the monoamine transporters. a, Sequence alignment of residues in TM1, TM3, TM6, and TM8 that constitute the substrate- or inhibitor-binding pocket of NET. **b-d,** Structural comparisons of NE-NET with DA-dDAT (**b,** PDB: 4XP1), 5-HT-SERT (**c,** PDB: 7LIA), and NE-dDAT (NET-like) (**d,** PDB: 6M0Z).

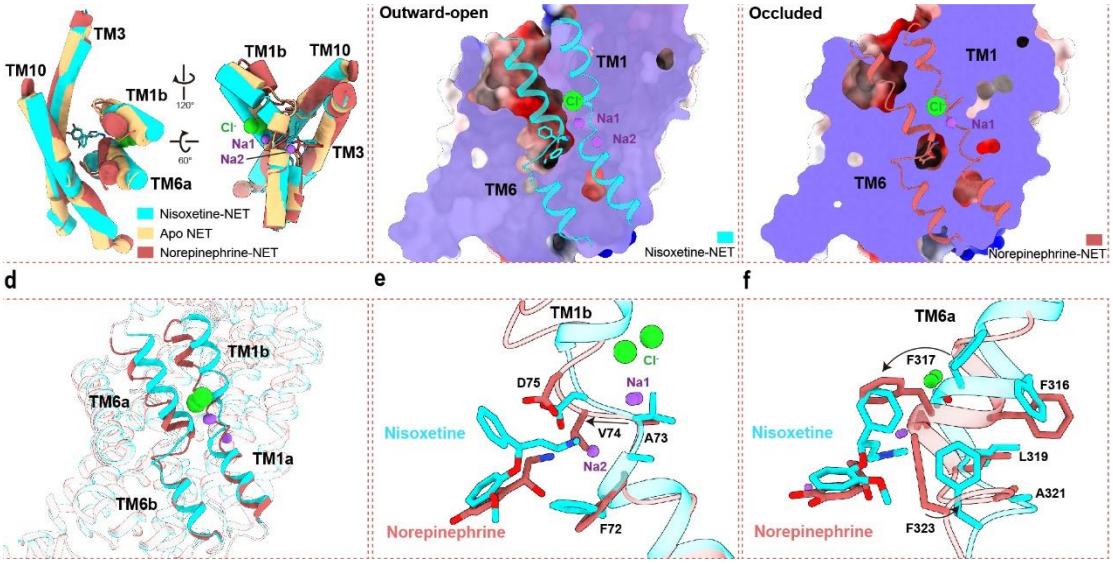

Extended Data Fig. 5| Norepinephrine transport by NET. a, Structural comparison of nisoxetine-NET, Apo NET, and norepinephrine (NE)-NET. **b,** Outward-open tunnel and a potential pathway for two Na+ and one Cl-. **c,** Outward-occluded tunnel and the NE-binding site. **d,** Structural comparison of TM1b and TM6a between outward-open and occluded states. **e,** Key residues for Na1 release. TM1b moves toward TM3 due to NE binding, then the V74 undergoes a flip and occupies the position of Na1. **f,** Key residues for NE binding at TM6a. TM6a moves toward TM3 due to NE binding, then the F317 and F323 undergo a flip and form hydrophobic interactions with NE.

a

NET	Nisoxetine	Atomoxetine	Maprotiline	Amitriptyline	Nomifensine	Nefopam
F72						
D75						
A145						
V148						
Y151						
Y152						
F317						
G320						
F323						
V325						
S419						
S420						
G423						
A477						
I481						

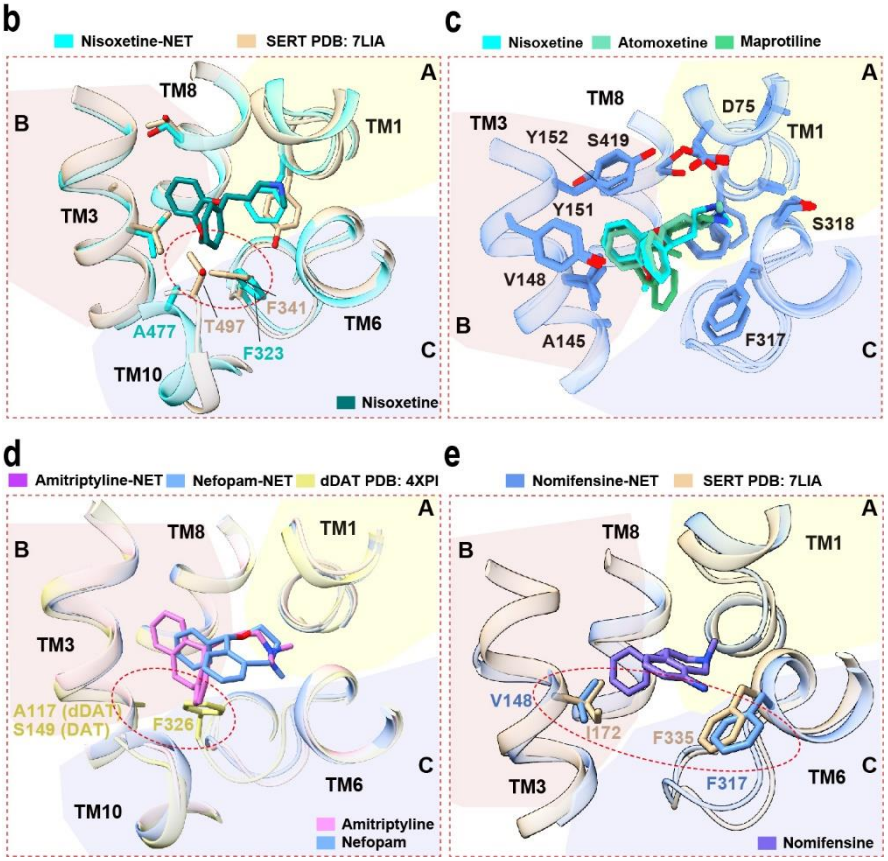

Extended Data Fig. 6| Recognition of antidepressants by monoamine transporters. **a,** The antidepressant-interacting residues (< 4 Å). **b-e,** Comparisons of binding modes of antidepressants. **b,** Structural superposition of nisoxetine bound NET and SERT (PDB: 7LIA). **c**, Binding mode comparison of nisoxetine, atomoxetine, and maprotiline in NET. **d**, Structural superposition of amitriptyline and nefopam bound NET and dDAT (PDB: 4XP1). **e,** Structural superposition of nomifensine bound NET and SERT (PDB: 7LIA). Subsites A, B, and C are highlighted by yellow, salmon, and light blue backgrounds, respectively. The potential clashes between antidepressants and SERT or dDAT were indicated by red dashed ovals.

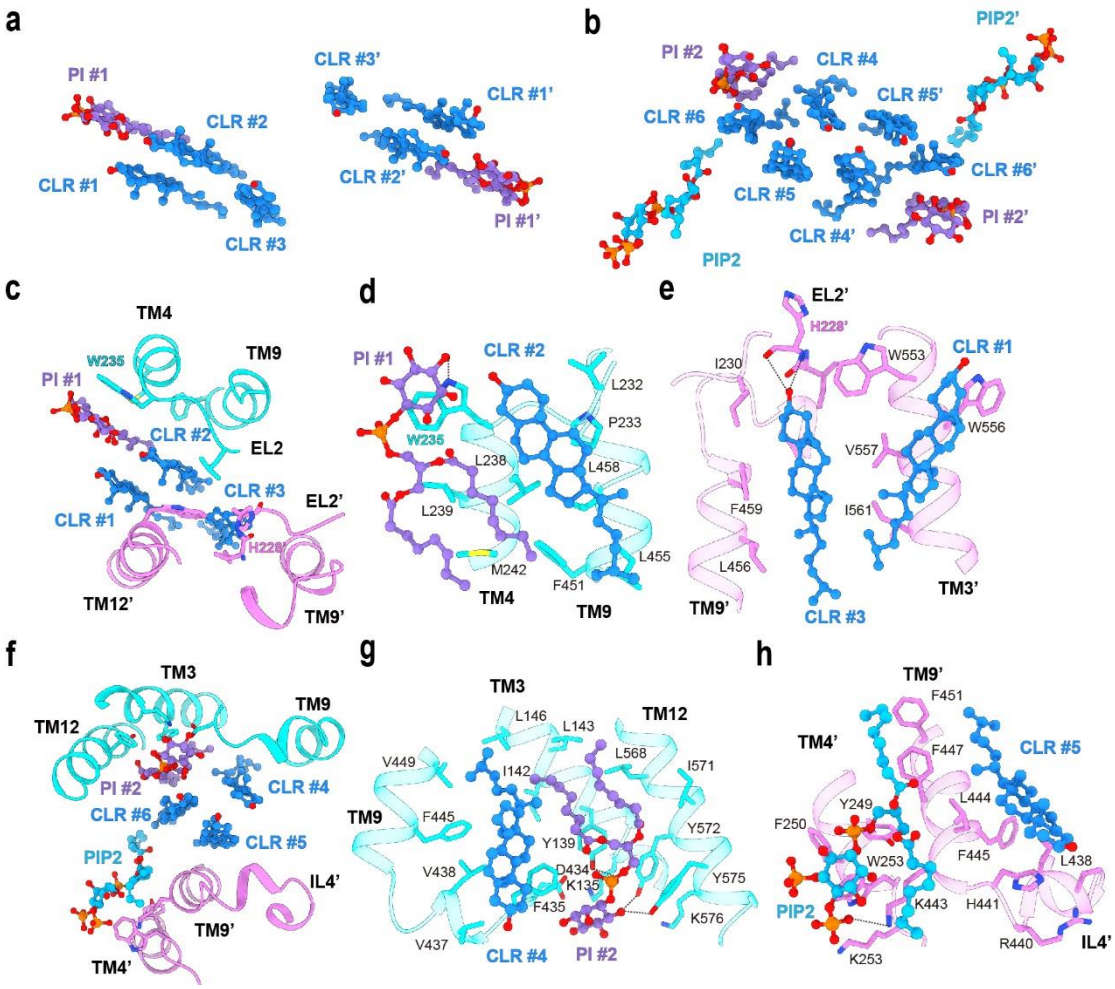

Extended Data Fig. 7| Binding details of cholesterols and lipids with residues at the homodimeric interface of NET. a, The two PIs (phosphatidylinositol) and six cholesterol molecules (CLRs) located at the upper layer interface from the extracellular view. **b,** The Six cholesterols, two PIs, two phosphatidylinositol 4,5-bisphosphate (PIP2) packed at the lower layer interface from the bottom view. **c-h,** Detailed interactions between specific CLR or lipid with residues at the homodimeric interface of NET. Cholesterol (dodger blue), PI (medium purple), and PIP2 (deep sky blue) are represented by the ball and stick (blue). The side chains of residues in two protomers of NET (cyan and purple) are shown by sticks.

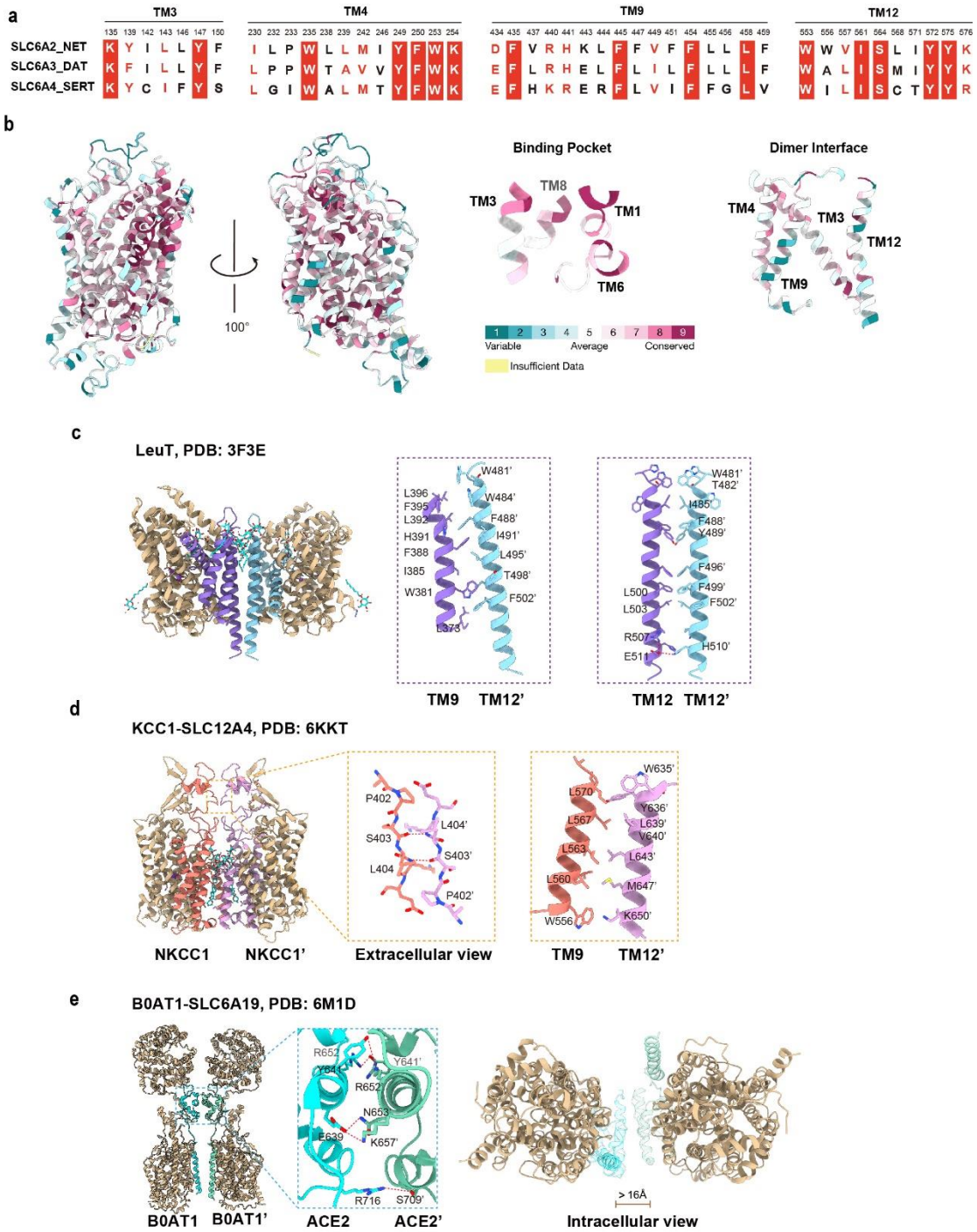

Extended Data Fig. 8 | The unique homodimeric mode of NET. a, Sequence alignment of residues in TM3, TM4, TM9, and TM12 at the homodimeric interface of NET. **b,** The sequence conservation between three monoamine transporters (NET, DAT, and SERT) in cartoon representation. The conservation is colored as indicated. The higher number stands for a higher conservation. **c-e,** Homodimeric interfaces of transporters with reported structures, including bacterial leucine transporter (**c,** LeuT, PDB: 3F3E), solute carrier family 12 member 4 (**d,** SLC12A4, PDB: 6KKT), and solute carrier family 6 member 19 (**e,** SLC6A19, PDB: 6M1D).

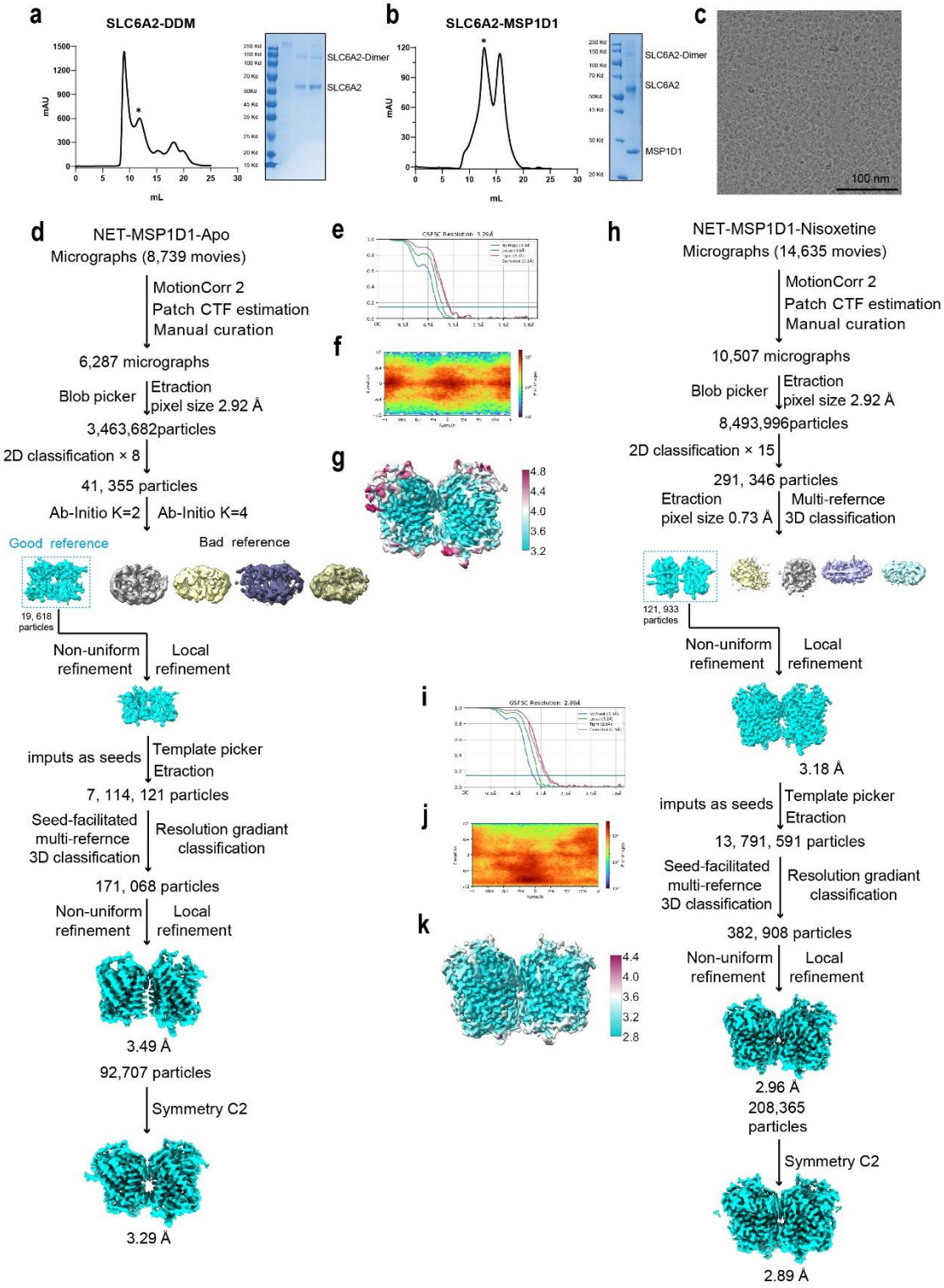

Supplementary Fig. 1| Nanodisc reconstitution and data processing of Apo NET and nisoxetine-NET. a, b, The size-exclusion chromatography evaluation and the SDS-PAGE analysis result of the NET in the detergent 0.02% DDM (**a**) and the NET reconstituted into MSP1D1 Nanodisc (**b**). **c,** Representative cryo-EM micrograph of Apo NET-MSP1D1, the scale bar located at the lower right. **d,** Data processing workflow of Apo NET-MSP1D1 by Cryosparc4.3.1 and ChimeraX. **e,** Gold-standard Fourier shell correlation (FSC) curve for

the 3D refinement of the overall structure of apo NET dimer. **f,** Angular distribution of the particles used for final reconstitution of the apo NET dimer. **g,** The local resolution of the sharpened map is calculated by Cryosparc4.3.1. **h,** Data processing workflow of nisoxetine-NET-MSP1D1 by Cryosparc4.3.1 and ChimeraX. **i,** Gold-standard Fourier shell correlation (FSC) curve for the 3D refinement of the overall structure of nisoxetine-NET dimer. **j,** Angular distribution of the particles used for final reconstitution of the nisoxetine-NET dimer. **k,** The local resolution of the sharpened map is calculated by Cryosparc4.3.1.

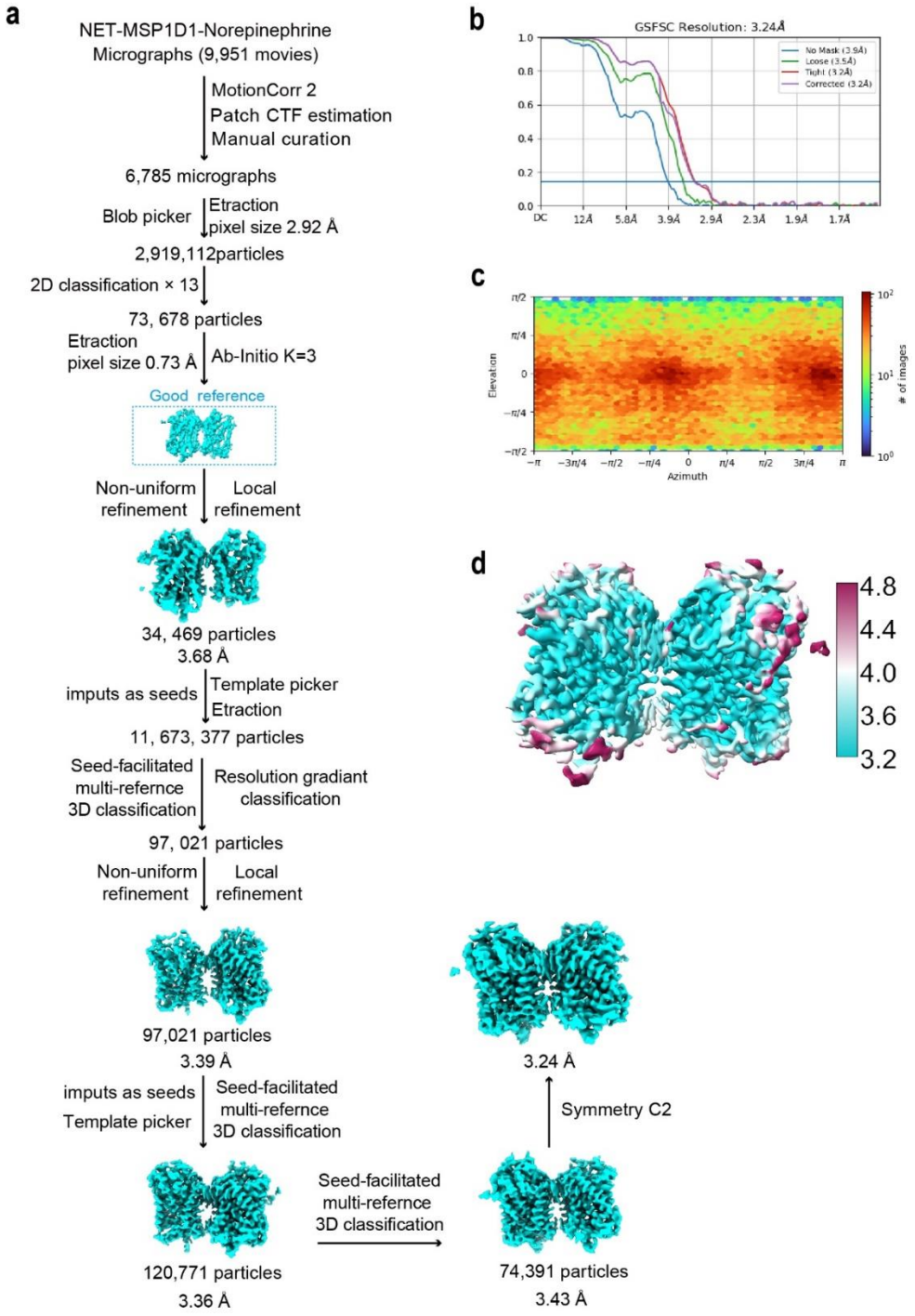

Supplementary Fig. 2| Data processing of Norepinephrine-NET. a, Data processing workflow of norepinephrine-NET-MSP1D1 by Cryosparc4.3.1. **b,** Gold standard Fourier shell correlation (FSC) curve for the 3D refinement of the overall structure of norepinephrine-NET dimer. **c,** Angular distribution of the particles used for final reconstitution of the norepinephrine-NET dimer. **d,** The local resolution of the sharpened norepinephrine-NET dimer map calculated by Cryosparc4.3.1.

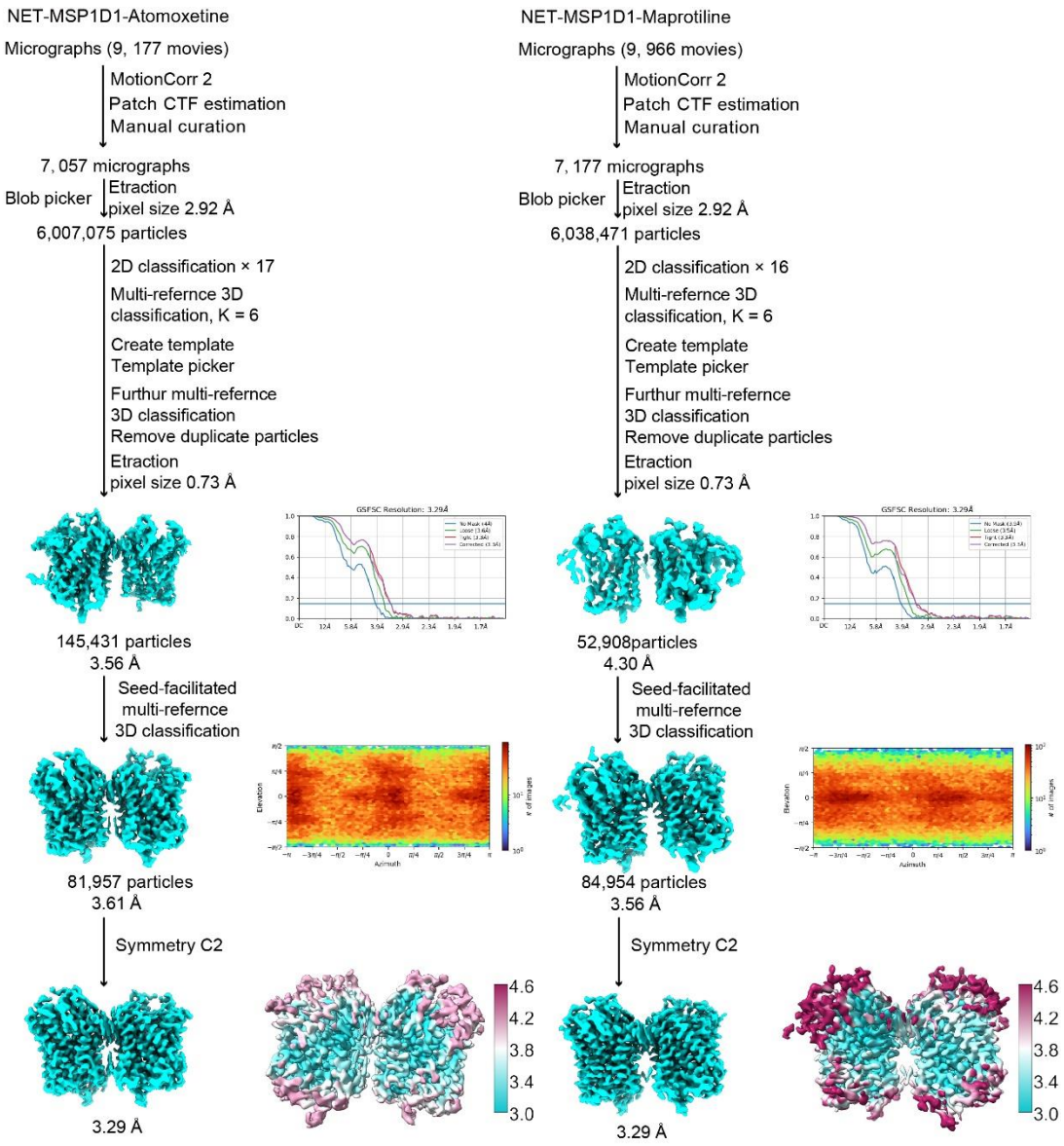

Supplementary Fig. 3| Data processing and structure determination of NET dimers bound with atomoxetine (Left) and Maprotiline (Right). The data processing workflow by Cryosparc4.3.1, Gold standard Fourier shell correlation (FSC) curve for the 3D refinement, Angular distribution of the particles used for final reconstitution of NET dimers, and the local resolution of the sharpened NET dimer maps calculated by Cryosparc4.3.1 are shown.

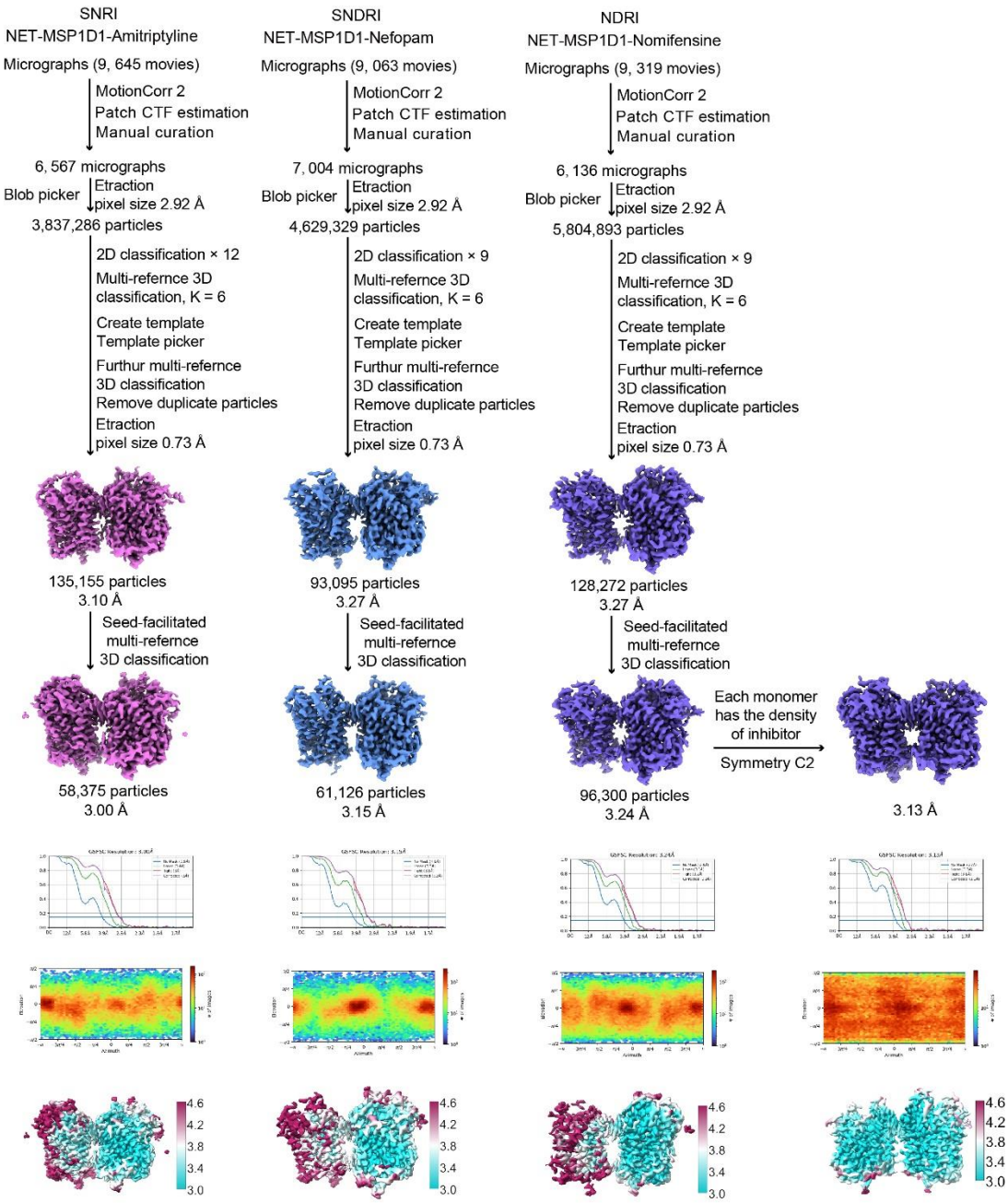

Supplementary Fig. 4| Data processing and structure determination of NET dimers bound with amitriptyline (left), nefopam (middle), and nomifensine (right). The data processing workflow by Cryosparc4.3.1, Gold standard Fourier shell correlation (FSC) curve for the 3D refinement, Angular distribution of the particles used for final reconstitution of NET dimers, and the local resolution of the sharpened NET dimer maps calculated by Cryosparc4.3.1 are shown.